OXFORD

A pH-response chemotherapy synergistic photothermal therapy for tumor suppression and bone regeneration by mussel-inspired Mg implant

Hongwei Shao[1,2,†], Shi Cheng[1,†], Mengyu Yao[1,†], Xiongfa Ji[1], Hua Zhong[3,*], Donghui Wang[4], Xiujuan Fan[5], Qian Li[1], Jielong Zhou[1,6], Yu Zhang[1,2,6,*] and Feng Peng [1,*]

[1]Department of Orthopedics, Research Center of Medical Sciences, Guangdong Provincial People's Hospital, Guangdong Academy of Medical Sciences, No. 106, Zhongshan 2nd Road, Yuexiu District, Guangzhou, Guangdong 510080, China [2]School of Medicine, South China University of Technology, Guangzhou University Town, Panyu District, Guangzhou, Guangdong 510006, China [3]Department of Orthopedics, The Fifth Affiliated Hospital of Southern Medical University, No. 566 Congcheng Avenue, Conghua District, Guangzhou, Guangdong 510900, China [4]School of Materials Science and Engineering, Hebei University of Technology, No. 5340 Xiping Road, Beichen District, Tianjin 300130, China [5]Department of Orthopedics, The Second School of Clinical Medicine, Southern Medical University, No. 111 Liuhua Road, Yuexiu District, Guangzhou, Guangdong 510515, China [6]Institute of New Materials, Guangdong Academy of Sciences, No. 363 Changxing Road, Tianhe District, Guangzhou, Guangdong 510651, China

*Correspondence addresses. The Fifth Affiliated Hospital of Southern Medical University, Guangzhou 510900, China. Tel: 86-15821598417;
E-mail: zhong8099@163.com (H.Z.); The Second School of Clinical Medicine, Southern Medical University, Guangzhou 510515, China. Tel: 86-13602744495; E-mail: zhangyu@gdph.org.cn (Y.Z.); Department of Orthopedics, Research Center of Medical Sciences, Guangdong Provincial People's Hospital, Guangdong Academy of Medical Sciences, Guangzhou, Guangdong 510080, China. Tel: 86-18616936841; E-mail: peng_feng7@163.com (F.P.)
[†]These authors contributed equally to this work.

Abstract

Primary malignant bone tumors can be life-threatening. Surgical resection of tumor plus chemotherapy is the standard clinical treatment. However, postoperative recovery is hindered due to tumor recurrence caused by residual tumor cells and bone defect caused by resection of tumor tissue. Herein, a multifunctional mussel-inspired film was fabricated on Mg alloy, that is, an inner hydrothermal-treated layer, a middle layer of polydopamine, and an outer layer of doxorubicin. The modified Mg alloy showed excellent photothermal effect and thermal/pH-controlled release of doxorubicin. The synergistic effect of chemotherapy and photothermal therapy enabled the modified Mg alloy to kill bone tumor *in vitro* and inhibit tumor growth in nude mice. Moreover, because of the controlled release of Mg ions and biocompatibility of polydopamine, the modified Mg alloy supported extracellular matrix mineralization, alkaline phosphatase activity, and bone-related gene expression in C3H10T1/2. Bone implantation model in rats verified that the modified Mg showed excellent osteointegration. These findings prove that the use of mussel-inspired multifunction film on Mg alloy offers a promising strategy for the therapy of primary malignant bone tumor.

Introduction

Primary malignant bone tumors often result in poor quality of life and low survival rate [1]. With the advances in surgery and the use of multidisciplinary approaches, the treatment of malignant bone tumors has shifted from amputation towards limb-salvage surgery (LSS) to improve life quality of patients [2, 3]. Results from a randomized controlled trial, which included 1330 patients, revealed that patients who received LSS had a higher 5-year survival rate than those who underwent amputation [4]. For LSS, the bone tumors are either inactivated and then removed or removed directly. The resultant bone defect area is then implanted with bone graft to accelerate bone reconstruction. However, the bone tumor cells are rarely removed completely, and the residual tumor cells often cause local relapse. Data on shoulder resection and reconstruction in patients with bone tumors from a cancer center in north-east India suggested that the relapse ratio of LSS can be as high as 25% [5]. Furthermore, the poor bone reconstruction for tumor-related bone defects often results in the failure of implants [6, 7]. Therefore, there is a need to develop novel orthopedic implants with antitumor and enhanced bone rebuilding capabilities as a rational strategy for the treatment of tumor-related bone defects.

Mg and Mg alloys are emerging as the next generation of biomedical metal implants owing to their biodegradability, suitable mechanical properties, and favorable bone regeneration enhancement effects [8–10]. Current orthopedic applications of Mg mainly include their use as screw and lamella in the fixation system of the normal bone defect or fracture models [11, 12]. In addition, studies are being conducted to broaden the application of Mg as orthopedic implants, for example, to treat tumor-related bone defects. There is evidence that the Mg ions released during Mg degradation can induce osteosarcoma cells apoptosis and inhibit its proliferation through a parallel antitumor signaling pathway of miRNA-181d-5p/TIMP3 and miRNA-181c-5p/NLK downstream. Simultaneously, the released hydrogen gas can eliminate intracellular excessive reactive oxygen species to suppress cell proliferation [13]. Other studies reported that even Mg implants were treated with anodic oxide, they still showed antitumor property *in vivo* [14, 15]. Another useful strategy using Mg to kill tumor cells is to deliver anti-tumor drugs. Li *et al.* loaded bisphosphonate on micro-arc oxidation treated-Mg alloy and zoledronic acid on Ca-P-treated Mg alloy [16, 17]. They observed that the as-prepared Mg alloys could significantly suppress tumor growth through inhibition of mevalonate pathway or NF-κB pathway. However, bare Mg and anodic oxide-treated Mg could not completely eliminate bone tumor, thus leaving a possibility of relapse. In addition, drug-loaded Mg could not precisely control the drug release rate. An excessive release of drug could damage the surrounding tissue. More importantly, these studies ignored the bone regeneration ability of Mg implants. Therefore, designing and fabricating Mg implants with controlled antitumor ability and enhanced osteointegration is of great importance for treating tumor-induced bone defects.

Mussel can tightly adhere on almost everything, such as boat, rock, and metal, which can be ascribed to its secretion of mytilusedulis foot proteins (Mefp) [18]. Dopamine has the similar function groups as Mefp and can be deposited on almost everything *via* self-polymeralization, and the finally product called polydopamine (PDA). Therefore, PDA is widely known as mussel-inspired function material [19]. PDA has a thickness of ∼100 nm and functional groups of catechol, amine, and imine. PDA has been deposited on biomedical Mg alloy for better corrosion resistance and biocompatibility [20, 21]. PDA coating is also reported as a general strategy to enhance osteogenic differentiation of orthopedic implants [22]. Furthermore, PDA is widely used in cancer diagnosis and therapy [23]. The structure of PDA is similar to melanin and its photothermal conversion efficiency under near-infrared (NIR) is approximately 40% [24, 25]. The functional groups of PDA can be used to load antitumor drugs and the drugs can be released in a sustained and pH-responsive manner [26]. Based on these assumptions, we attempted to fabricate a multifunctional coating on Mg alloy with the aid of PDA for tumor-induced bone defects treatment.

Herein, a hydrothermal treatment coating was first prepared on AZ31 alloy to provide basic corrosion protection [27, 28]. PDA was then deposited on the hydrothermal-treated AZ31 and finally loaded with antitumor drug doxorubicin (Dox). The photothermal effect and drug release rate were evaluated. The antitumor and osteogenesis performances of the multi-layer coating were investigated *in vitro* and *in vivo*.

Materials and methods

Sample preparation and characterization
AZ31 alloys were cut into dimensions of $\varnothing$ 10 mm × 2 mm (for *in vitro* tests), $\varnothing$ 2 mm × 10 mm (for bone implantation), and $\varnothing$ 2 mm × 4 mm (for tumor implantation). AZ31 plates were put in a Teflon-lined stainless containing 50 ml $Al(NO_3)_3$ solution (0.02 M, pH adjusted to 12.8 with NaOH). The Teflon-line stainless was kept at 120°C for 12 h and the obtained samples were denoted as LDH#.

Fifty milligrams dopamine-HCl were dissolved in 10 ml Tris-HCl solution (10 mM, pH 8.5). LDH# samples were immersed in the dopamine solution at 37°C for 12 h. The dopamine coating process was repeated three times and the obtained samples were denoted as L-P#. Next, L-P# samples were immersed in Dox solution (50 μM) for 12 h and the obtained sample was rinsed with ultrapure water and denoted as L-P-D#. When the Dox concentration was increased to 75 μM, the obtained sample was found to be cytotoxic to 143b cells under normal culture conditions (Supplementary Fig. S1). Therefore, we selected a Dox concentration of 50 μM to fabricate L-P-D# samples for the subsequent experiments.

The surface views of the samples were observed using scanning electron microscopy (Hitachi-S3400N, Hitachi, Japan). The phase compositions were detected by X-ray diffraction (XRD; D/Max, RIGAKU, Tokyo, Japan) and chemical element compositions were detected using X-ray photoelectron spectroscopy (XPS; PHI 5802, Physical Electronics Inc., USA).

Electrochemical evaluation
Electrochemical analysis was conducted using a CHI760C electrochemical analyzer (Shanghai, China) with a three-electrode electrochemical cell. Phosphate buffer saline (PBS) was used as the electrolyte. The samples were stabilized in PBS to get a stable open circuit potential prior to the test. Potentiodynamic polarization (PDP) measurements were done at a sweep rate of 10 mV·s^{-1}. The corrosion potential (E_{corr}), current density (j_{corr}), and corrosion resistance (R_p) were determined by Tafel extrapolation.

Photothermal effects of PDA coated samples

The photothermal properties of the samples were evaluated in a 24-well culture plate under dry (air) and wet (500 μl of PBS) conditions using an 808 nm laser beam (diameter: 12 mm). Temperature changes and thermal images of different samples (AZ31, LDH#, L-P# and L-P-D#) under NIR irradiation (1.19 W) were monitored in real-time and recorded by an infrared thermal thermography system.

Evaluation of drug release

The samples were placed in 24-well plates containing 1 ml of PBS with different pH values (7.4, 6, 4), which were adjusted using 0.01 M HCl. At scheduled time points, PBS was collected and then the 24-well plates were replaced with fresh PBS. The Dox concentration in the collected PBS sample was measured at a wavelength of 480 nm using an UV−vis spectrophotometer (Lambda 750, Perkin Elmer, USA).

The samples were placed in 24-well plates containing 1 ml of PBS (pH = 7.4). At scheduled time points, the samples were irradiated with NIR (power: 0.74 and 1.19 W) for 10 min. Next, PBS was collected and then the 24-well plates were replaced with fresh PBS. The Dox concentration in the collected PBS sample was measured using an UV−vis spectrophotometer.

Cell culture

The 143b and C3H10T1/2 cell lines were purchased from American Type Culture Collection (ATCC). The 143b cells were cultured in high glucose Dulbecco's Modified Eagle Medium (DMEM) containing 10% fetal bovine serum (FBS; Gibco, USA) and 1% antibiotics. C3H10T1/2 cells were incubated in minimum essential media (MEM) containing 10% FBS and 1% antibiotics (100 U/ml penicillin and 100 μg/ml streptomycin; Gibco, USA) as well as 1% glutamine and 1% sodiumpyruvate, under standard conditions (37°C, 5% CO_2, and 100% humidity).

Photothermal effects of PDA coated sample on the viability of bone tumor cells

2.6.1 Cell viability under normal culture conditions

The 143b cells (3×10^4 cells/well) were seeded on the samples for 4 days. Next, the culture medium was replaced by 500 μl of Cell Counting Kit-8 (CCK-8) working agents and further cultured for 2 h. Thereafter, the working agents were removed into a 96-well plate and the optical density values at 450 nm were detected using an enzyme labeling instrument (BIO-TEK, ELX 800).

Cell viability and live/dead staining under low pH value and NIR irradiation

The pH value of DMEM was adjusted to 6 using HCl solution. The 143b cells were seeded on L-P-D# sample. The samples were divided into four groups according to the culture conditions: (i) pH = 7.4 without NIR irradiation, (ii) pH = 6 without NIR irradiation, (iii) pH = 7.4 with NIR irradiation, and (iv) pH = 6 with NIR irradiation. The cells were cultured for 24 h and later subjected to 10-min NIR irradiation (1.19 W). The cell viability was measured by CCK-8 assay. Next, the cells were washed with PBS and then incubated with calcein AM to stain live cells and propidium iodide to stain dead cells following the manufacturer's instruction. The stained cells were observed using a fluorescence microscope (Olympus IX 71, Olympus, Japan).

Photothermal effects of PDA coated sample on *in vivo* tumor therapy

All the procedures in the animal experiments were approved by the Guidelines for Care and Use of Laboratory Animals of South China University of Technology and Animal Ethics Committee of Guangdong Provincial People's Hospital.

UMR106 tumor cells (1×10^6 cells) were subcutaneously injected into the backs of Balb/c nude mouse (male, 4–6 weeks old). When the tumor volume reached 500 mm^3, the mice were randomly divided into six groups ($n = 5$): (i) control group; (ii) LDH# group; (iii) L-P# group; (iv) L-P-D# group; (v) L-P# + NIR group; (vi) L-P-D# + NIR group. Skin incisions were made at the edge of the tumors and the samples were implanted into the center of the tumors. For the NIR treatment groups, each mouse was exposed to the NIR laser (1.58 W cm^{-2}, 5 min), and the tumor surface temperature was recorded. The day of the first NIR treatment was defined as Day 0. The length and width of each tumor were measured using caliper every day. Tumor volume was calculated using the following formula: Tumor volume (TV) = (length × width^2)/2. The relative tumor volumes (Vr) were calculated as follows: $Vr = V/V0$ ($V0 =$ tumor volume on Day 0).

The mice were sacrificed on 7th day and all tumors were harvested and photographed. The tumors were then fixed in 4% neutral buffered formalin, embedded in paraffin, sectioned, stained with hematoxylin and eosin (H&E), and observed using an optical microscope (Leica, DM4000B). The sections were also subjected to immunofluorescent staining with Ki67 and deoxynucleotidyl transferase-mediated dUTP nick-end labeling (TUNEL) and analyzed using a fluorescence microscope (GX71, Olypus, USA). Moreover, the essential organic tissues, including liver, kidney, heart, spleen, and lung, were collected for H&E staining.

In vitro osteogenic differentiation of C3H10T1/2 for PDA coated samples

Extracts were collected to evaluate the biological effects of various samples. The samples were immersed in MEM for 24 h with an area-medium ratio of 1 cm^2/ml. The harvested extracts were added with 10 mM β-glycerophosphate, 100 nM dexamethasone, 50 mM ascorbate and glutamine. These extracts were then used for the subsequent osteogenic differentiation experiments.

Alkaline phosphatase (ALP) activity assay

C3H10T1/2 cells (2×10^4 cells/well) were seeded in 12-well culture plates for 1 day and then the culture medium were replaced by the various extracts. After further cultured for 3 and 7 days, the expression of ALP was stained using the BCIP/NBT ALP color development kit (Beyotime, China) and the intracellular ALP activities were quantitatively assayed using ALP Assay Kit (Beyotime Biotechnology, China). Total protein was measured by BCA protein quantitation kit (Beyotime, China). The ALP activity was normalized with total protein content.

Extracellular matrix (ECM) mineralization

ECM mineralization of C3H10T1/2 was analyzed with Alizarin Red staining. After culturing in the extracts for 7 and 14 days, the cells were fixed with 75% ethanol for 1 h and subsequently stained with 2% Alizarin Red solution (Cyagen, China). Images were taken by an optical microscope (Olympus, Germany). The bonded dyes were dissolved in 10 mM sodium phosphate aqueous solution containing

cetylpyridinum chloride (Sigma-Aldrich, USA) and the absorbance was measured at 540 nm with a microplate reader (Bio-Tek, USA).

Quantitative real-time polymerase chain reaction (qRT-PCR) assay
C3H10T1/2 cells (2.5×10^5 cells/well) were cultured in various extracts for 3 and 7 days. Then, the total RNA of C3H10T1/2 was purified by the Total RNA Kit (Omega). The standard cDNA was synthesized using the first strand cDNA synthesis supermix Kit (Yeasen, China). The synthesized cDNA was then mixed with SYBR Green Supermix and primers and qRT-PCR programs were run on a CFX Connect Real-Time PCR Detection System (BIO-RAD, USA). Data were analyzed according to the $2^{-\Delta\Delta CT}$ method. The expression of osteogenesis-related genes, including collagen-I (COL-I), osteocalcin (OCN), osteopontin (OPN), and runt-related transcription factor-2 (RUNX-2), were detected and normalized to glyceraldehyde-3-phosphate dehydrogenase. The involved primer sequences are listed in Supplementary Table S1.

In vivo bone regeneration for PDA coated samples
Animal surgery
Eight adult male Sprague Dawley rats ($\sim$200 g) were used to evaluate the osteointegration of different samples. The rats were anesthetized using 3% pentobarbital sodium solution. Then, the mid-shaft of femur was exposed through a lateral longitudinal skin incision and tunnels (2 mm in diameter) were drilled from the patellofemoral groove of the distal femur along the axis of the femoral shaft. The sterilized rods were inserted into the femur canal. Next, deep fascia and skin were sutured layer by layer. Each rat was intramuscularly injected with prophylactic antibiotics to prevent infection.

Micro computed tomography (micro-CT) analysis and histological examinations
The rats were sacrificed at week 8 after surgery. The femora were fixed in formalin. Micro-CT (Aloka Latheta LCT-200; HITACHI, Japan) scans were applied under 80 kV and 40 μA. The obtained radiographic images were reconstructed into three-dimensional (3D) images using Multimodal 3D Visualization (Siemens, Germany) software. The bone volume percentage (BV/TV) within a region of interest and the bone mineral density (BMD) were also measured. Thereafter, the specimens were dehydrated with increasing concentration of ethanol and polymethyl methacrylate was used for embedding the specimens. The embedded specimens were treated with a cutting grinding system (EXAKT Apparatebau, Nordestedt, Hamburg, Germany). The tissue sections were stained with Van Geison's solution (VG) for histological analysis and observed under a microscope (Olympus, Germany).

Statistical analysis
The data were expressed as mean $\pm$ standard deviation and all experiments were performed at least three times. Statistical analysis was performed using one-way analysis of variance using GraphPad Prism 6. Values of * ($P < 0.05$) were considered statistically significant (*$P < 0.05$, **$P < 0.01$, ***$P < 0.001$, ****$P < 0.0001$) [29].

Results and discussion

Coating characterization and corrosion resistance evaluation
The surface morphologies of different samples are shown in Fig. 1a. Scratches caused by sandpaper can be seen clearly on the surface of AZ31. After hydrothermal treatment, the surface was covered by a layer of micro-nano flake structures (LDH#). Further coated with PDA and bonded with Dox on LDH# surface had no influence on the morphology. Figure 1b shows the XRD patterns of the samples. Characteristic peaks of only Mg were detected in AZ31 sample. The XRD patterns of LDH#, L-P#, and L-P-D# were similar to each other. Specially, in addition to the detection of the characteristic peaks of Mg, peaks were also detected at 12° and 18°, which represented the formation of LDH and $Mg(OH)_2$ phases, respectively. Figure 1c shows the full XPS spectrum of the samples and the quantitative results of the element compositions are shown in Table 1. Mg and Al elements were detected on LDH# sample which confirmed the LDH structure on its surface is Mg-Al LDH. Moreover, significant N peaks were observed for L-P# and L-P-D# samples, suggesting the successful deposition of PDA coating. The N content of L-P-D# was two times greater than that of L-P# sample because Dox on L-P-D# surface also contained N element.

Figure 1d shows the PDP curves of the samples, and the corresponding corrosion data are presented in Table 2. Compared with bare AZ31 sample, the j_{corr} values of all modified samples decreased by two orders of magnitude, while the R_p values increased by two orders of magnitude, indicating that the corrosion resistances of all modified samples were greatly improved. Furthermore, the j_{corr} values of PDA coated samples (L-P# and L-P-D#) were lower than that of LDH#, whereas the R_p values in contrast, demonstrating that PDA could further enhance the corrosion resistance of hydrothermal-treated sample. Results from our previous studies have confirmed that LDH coating can improve *in vitro* and *in vivo* corrosion resistance of Mg-based materials [27, 30]. PDA is a compact layer of polymer that can effectively prevent the penetration of liquid molecules and block the electron transfer between Mg substrate and corrosive solution, thus improving the corrosion resistance of the material [21, 31, 32].

Figure 2 displays the photothermal properties of various samples. In a dry environment, the surface temperature of AZ31 only increased to 37°C after 5 min of NIR irradiation, while LDH#, L-P#, and L-P-D# groups increased to 55°C, 63°C, and 65°C, respectively (Fig. 2a). In a wet environment, after 10 min of NIR irradiation, the surface temperature of PDA-modified samples was approximately 10°C higher than that of AZ31 sample and 2°C higher than that of LDH# sample (Fig. 2b). These results suggested that PDA coating could enhance photothermal performance of hydrothermal-treated sample even in a wet condition. We further investigated the release profile of Dox from L-P-D# sample (Fig. 3). As shown in Fig. 3a, the concentration of Dox released from L-P-D# increased with the decrease of pH value. Moreover, as the irradiation power increased, the release of Dox also increased (Fig. 3b). This could be explained by the protonation of the amino group and catechol in PDA at a low pH value, which in turn reduced the binding force between PDA and Dox, leading to the increased release of Dox [33–35]. Part of the Dox was adsorbed on L-P-D# through electrostatic and nonpolar interaction. Under NIR irradiation, the surface temperature increased, causing the rapid diffusion of the adsorbed Dox into the solution [36, 37]. Hence, L-P-D# sample could respond to the acidic microenvironment and NIR stimulation to release Dox.

In vitro and *in vivo* antitumor abilities of L-P-D# sample
Human osteosarcoma cell line 143b was used as a model to investigate the *in vitro* anticancer effects of the samples. Figure 4a shows the viability of 143b cells cultured on various surfaces. The cells cultured on LDH# and L-P# exhibited a same level of viability. After
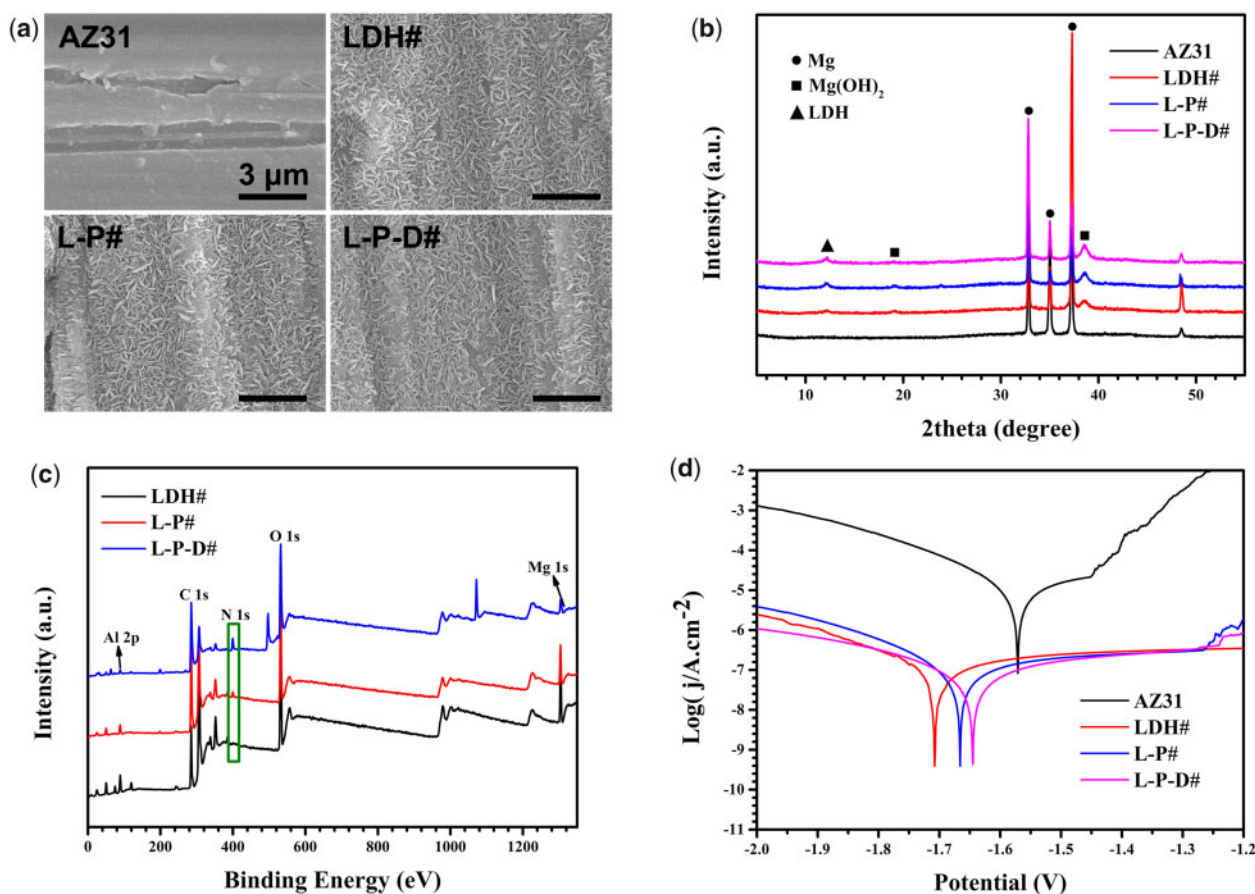
Figure 1. Surface views (a) and XRD patterns (b) of AZ31, LDH#, L-P#, and L-P-D# samples. XPS full spectra of LDH#, L-P#, and L-P-D# samples (c), and potentiodynamic polarization curves (d) of AZ31, LDH#, L-P#, and L-P-D# samples.

Table 1. Elemental compositions of LDH#, L-P# and L-P-D# samples, as detected by XPS

	Mg (at%)	O (at%)	C (at%)	Al (at%)	N (at%)
LDH#	14.37	28.93	47.81	8.08	0.8
L-P#	7.59	15.5	73	0.87	3.04
L-P-D#	1.63	21.97	68.64	1.27	6.49

Table 2. Corrosion data of the samples

	E_{corr} (V)	j_{corr} (A/cm^2)	R_p (Ω)
AZ31	−1.57	8.50×10^{-6}	1.15×10^5
LDH#	−1.7	8.05×10^{-8}	1.11×10^7
L-P#	−1.67	6.52×10^{-8}	1.55×10^7
L-P-D#	−1.64	4.50×10^{-8}	2.29×10^7

bonding Dox to the surface, cell viability decreased to ∼70%, suggesting that Dox was cytotoxic to 143b cells to an extent. Nevertheless, the living cells on L-P-D# sample still proliferated and covered the surface (Supplementary Fig. S1). Figure 4b shows the results of cell viability of the cells cultured on L-P-D# under various conditions. The 143b cells cultured in culture medium with a low pH value exhibited lower cell viability than that cultured at normal pH value. Under NIR irradiation, cytotoxicity was observed for cells cultured on L-P-D#, especially in case of the group that used a culture medium with pH 6. This trend was more vividly displayed in the result of live/dead staining. As shown in Fig. 4c, without NIR irradiation, almost no dead cells were observed for the group at pH 7.4; however, few dead cells and lower living cell density were observed for the group at pH 6. For the samples irradiated with NIR, a large number of dead cells were found at pH 7.4 and no living cells were found at pH 6. These results revealed that L-P-D# sample caused thorough ablation of 143b cells in an acidic environment with NIR irradiation due to the combination of thermaltherapy and chemotherapy.

To evaluate the *in vivo* anti-tumor effects of L-P-D# sample, a xenograft subcutaneous tumor model was established in Balb/c nude mice and then the samples with size of ∅ 2 mm × 4 mm were implanted into the central region of the tumors. As shown in Fig. 5a and b, the temperature surrounding L-P# and L-P-D# samples' implants could reach the highest value of 55°C after irradiation for 4 min. The changes in tumor volume and final tumor optical pictures are shown in Fig. 5c and d, respectively. The groups without NIR irradiation exhibited gradual increase in tumor size and were 3–4 times of the initial volumes. In contrast, in case of the NIR irradiated groups, the tumors showed decreased size, and the final tumor volumes were only one-third of the initial volumes. Evaluation of the tumor weight further confirmed this result (Supplementary Fig. S2). These data suggested that L-P# and L-P-D# implants could significantly suppress the growth of tumor under NIR irradiation. In addition, the tissues surrounding the implants were subjected to immunofluorescence staining. Ki67 is a cell proliferation-associated
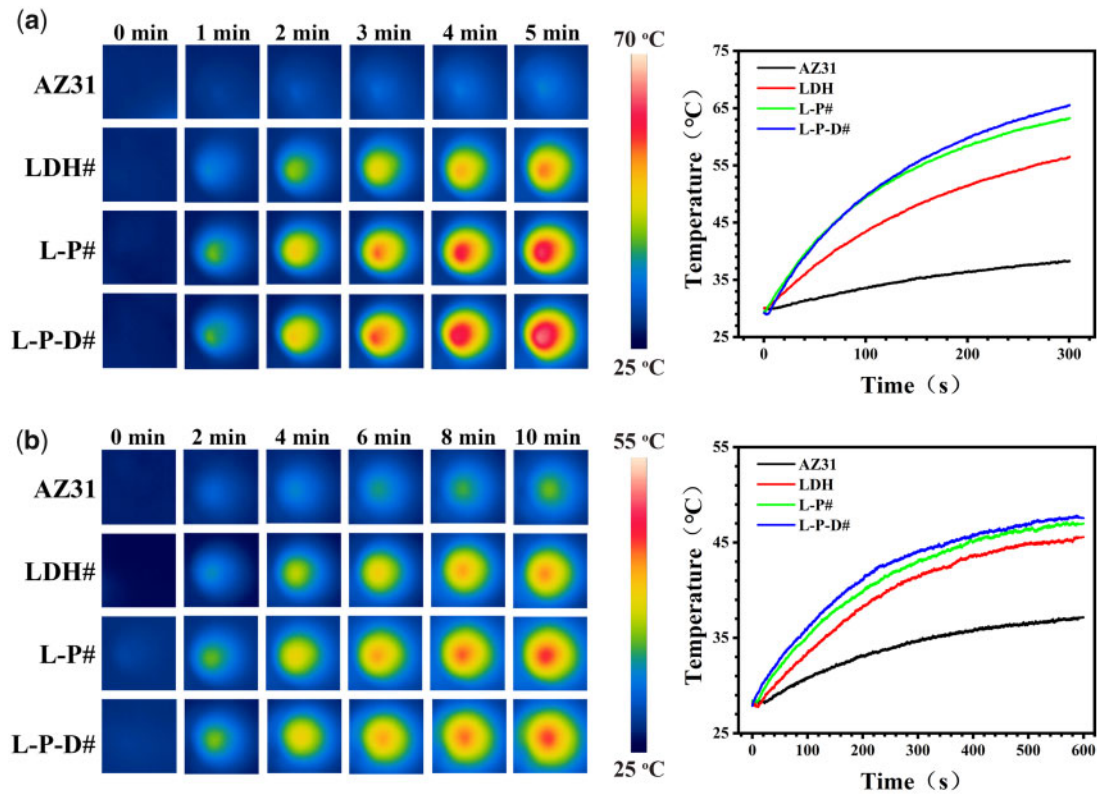
Figure 2. Thermal images and heating curves of the samples in the dry state under 1.19 W NIR irradiation for 5 min (a), and in PBS under 1.19 W NIR irradiation for 10 min (b).
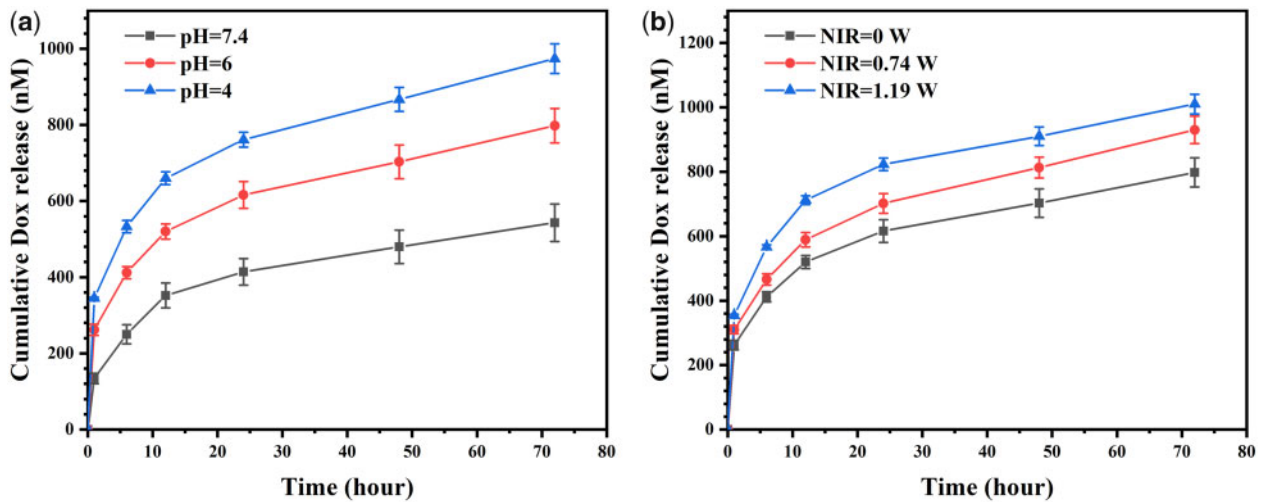

Figure 3. Release curves of Dox from L-P-D# sample in PBS at different pH values under 1.19 W NIR irradiation (a) and in PBS (pH = 7.4) under NIR irradiation with different powers (b).

antigen which is closely related to cell mitosis and is widely used in the clinic to label cells in the proliferative cycle [38, 39]. L-P-D# and L-P#+NIR groups showed a similar Ki67 expression level as the control, LDH#, and L-P# groups (Fig. 6a). However, for L-P-D#+NIR group, the expression level of Ki67 was significantly lower than the other groups. These results suggested that only hyperthermia or chemotherapy did not influence the proliferation of tumor

cells, but their synergistic therapy could dramatically inhibit tumor proliferation. Though L-P# group could inhibit tumor growth under NIR irradiation (Fig. 5c and d), the proliferation capability of the residual tumor cells was active. Hence, there was high chance that the tumor could quickly recur once NIR irradiation was discontinued. TUNEL assay was used to investigate apoptosis of tumor cells and the result is displayed in Fig. 6b. Few apoptotic cells were observed
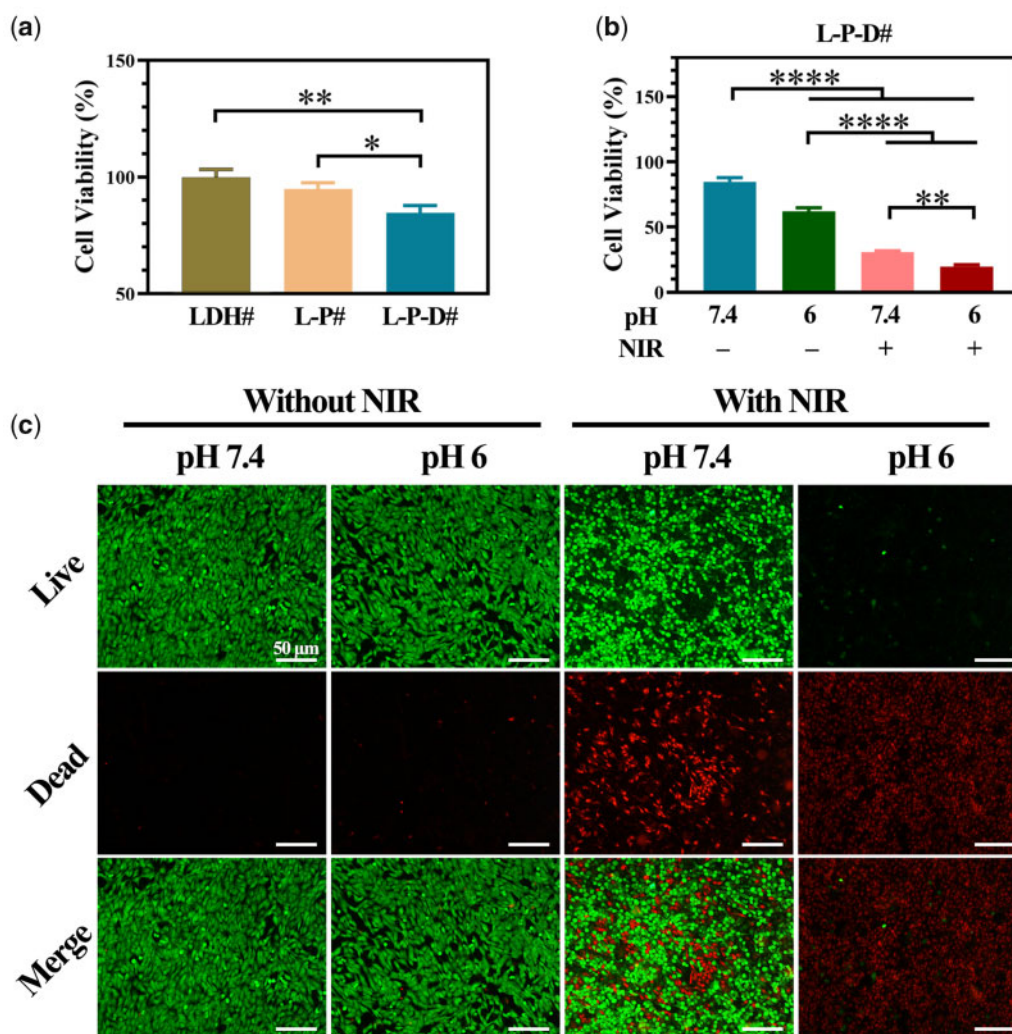
Figure 4. Cell viability of 143b cells cultured on LDH#, L-P#, and L-P-D# samples for 1 day (a); cell viability of 143b cells cultured on L-P-D# sample for 1 day under different culture conditions and the corresponding live/dead staining (c); LDH# group as control for the calculation of cell viability (*$P < 0.05$, **$P < 0.01$, ***$P < 0.001$, **** $P < 0.0001$).

in control, LDH#, and L-P# groups. As for L-P-D# and NIR irradiation groups, a large number of apoptotic cells were detected, suggesting that either hyperthermia/chemotherapy or their combination therapy could induce tumor cell death. Moreover, immunohistochemistry of vascular endothelial growth factor in each group indicated that L-P-D#+NIR group exhibited less angiogenesis, suggesting poor tumor growth (Supplementary Fig. S3). This further confirmed the tumor ablation ability of L-P-D# implant under NIR irradiation. We further evaluated the biosafety of the samples by analyzing the pathology of major organs, including the liver, kidney, heart, spleen, and lung (Supplementary Fig. S4). Results from H&E staining showed no obvious inflammation lesions or impairment in any group.

As a promising next-generation biomaterial, Mg-based implant is widely explored in orthopedic fields for bone defect therapy [40, 41]. In the past few years, increasing number of researchers have paid attention to the application of Mg in bone tumor. Both untreated and drug loaded Mg alloys have been explored as bone implant material after tumor resection [16–18]. However, in the case of uncoated Mg, the fast release of hydrogen gas and accumulation of hydroxyl ions are disadvantage for bone regeneration. In the

case of drug loaded Mg, the release of drug is difficult to control and an excessive release may damage normal tissue cells. In this study, LDH film was first prepared on AZ31 to provide corrosion protection, and then Dox was loaded through PDA layer. PDA film provided triple benefits as follows: (i) PDA formed a compact layer which further enhanced corrosion resistance of the materials; (ii) PDA acted as a photothermal conversion agent to provide thermal therapy; and (iii) The functional groups on PDA could be used to load Dox and thereby respond to acid microenvironment and NIR irradiation to release Dox. Therefore, the novel designed L-P-D# sample enabled the integration of hyperthermia and chemotherapy together for tumor treatment.

The *in vitro* and *in vivo* osteogenesis of L-P-D# sample

After ablation of residual bone tumor cells, the reconstruction of bone defect is another challenge for the implants. The *in vitro* and *in vivo* osteogenesis ability of L-P-D# sample was investigated *via* culturing C3H10T1/2 and using a bone implantation model in rats, respectively.
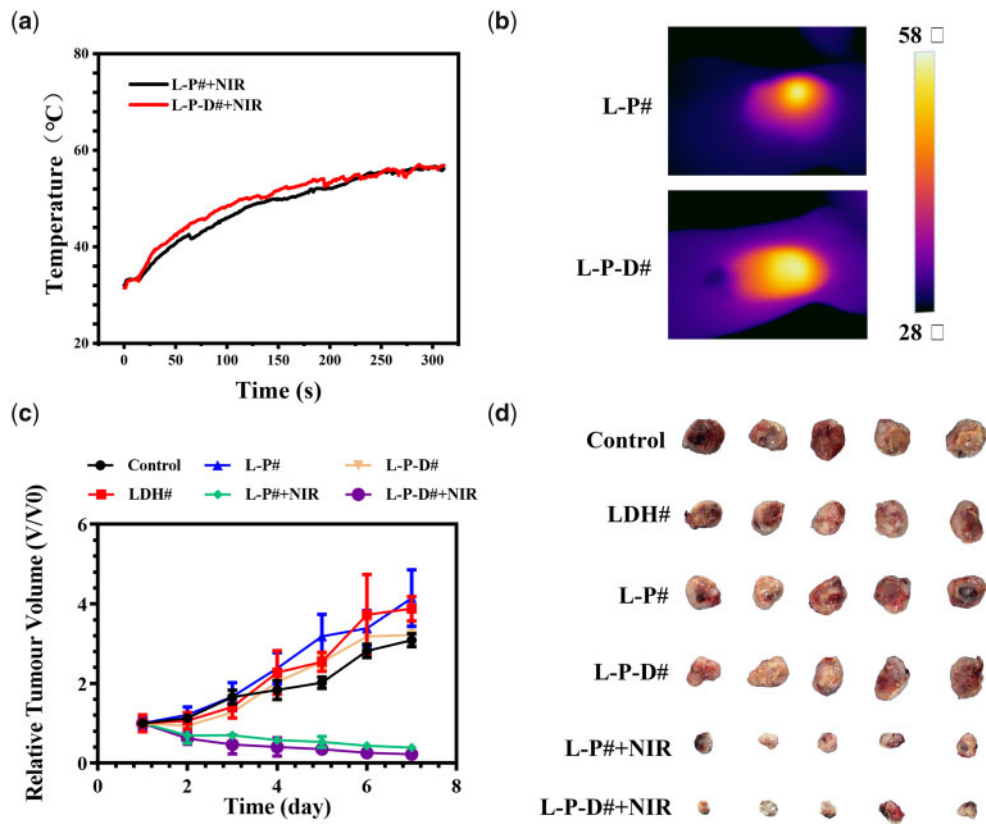
Figure 5. The real-time monitoring temperature changes in nude mice after implanted with L-P# and L-P-D# samples under 1.58 W NIR irradiation for 5 min (a) and the corresponding thermal images (b); relative volume changes of the tumors (c) and optical images of collected tumor tissues (d).
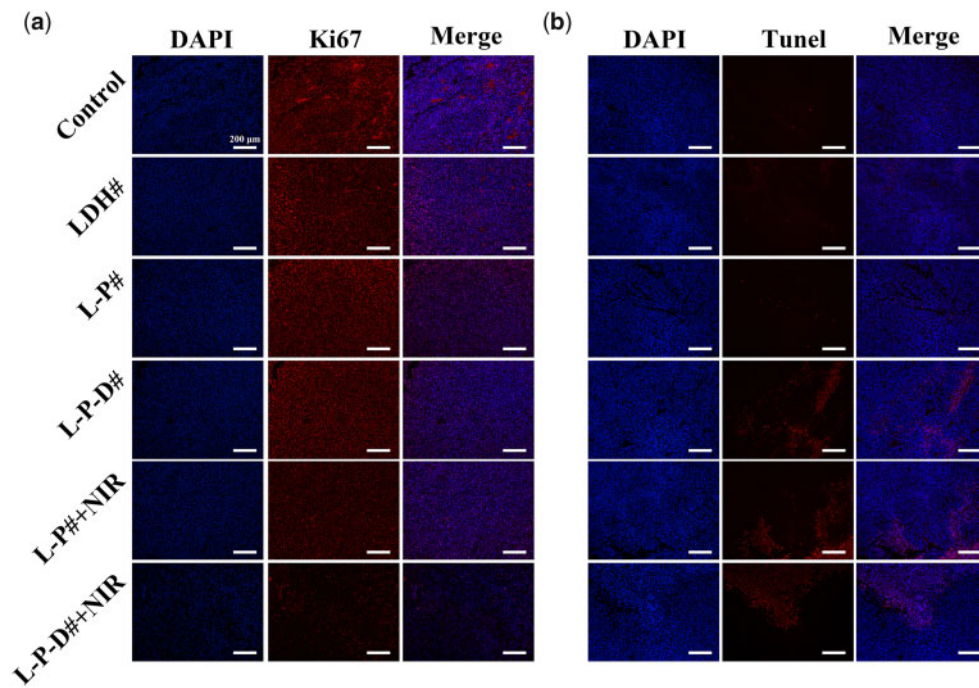

Figure 6. Ki67 (a) and Tunel (b) immunofluorescent staining of tissues collected from control, LDH#, L-P#, L-P-D#, L-P# + NIR, and L-P-D# + NIR groups after 7 days of implantation.
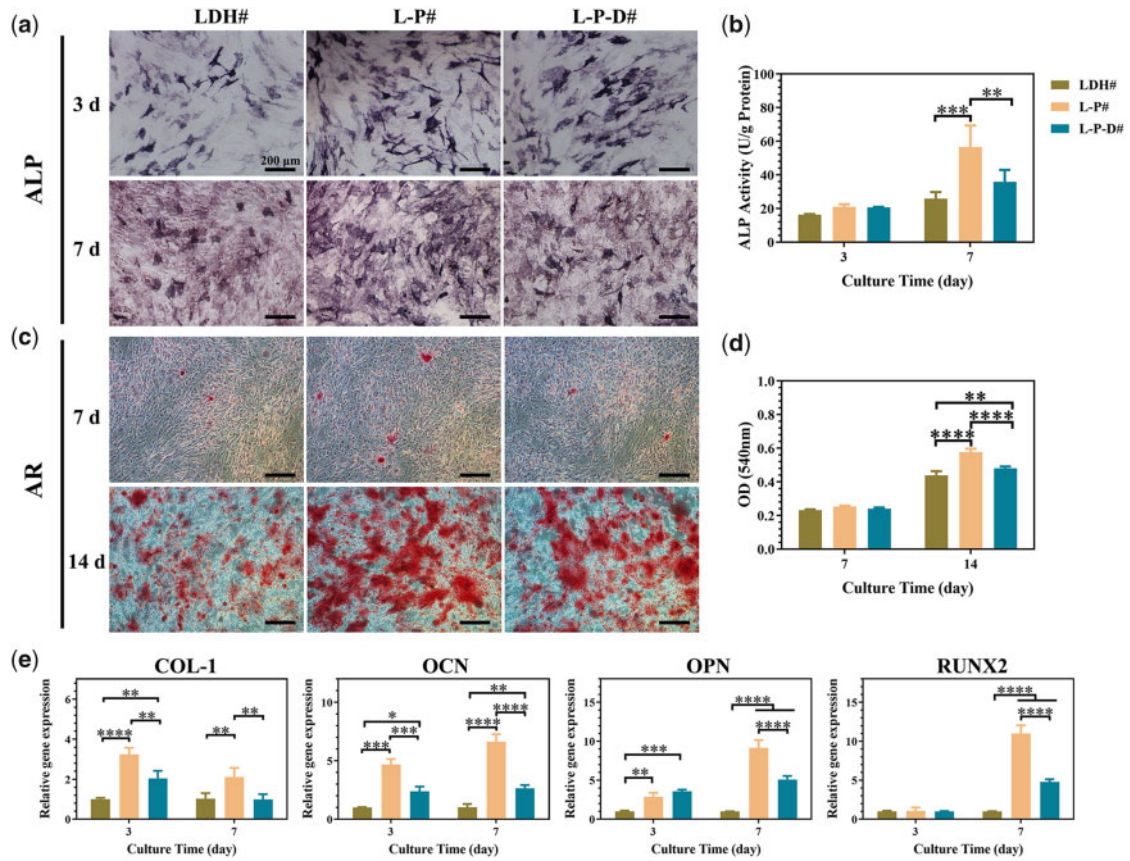
Figure 7. Staining area of ALP activity and corresponding quantitative results of C3H10T1/2 cells cultured in LDH#, L-P#, and L-P-D# extracts for 3 and 7 days (a and b); ECM mineralization and corresponding quantitative results of C3H10T1/2 cells cultured in LDH#, L-P#, and L-P-D# extracts for 7 and 14 days (c and d); expression of osteogenesis-related genes in C3H10T1/2 cells cultured in LDH#, L-P#, and L-P-D# extracts for 3 and 7 days (e) (*$P < 0.05$, **$P < 0.01$, ***$P < 0.001$, ****$P < 0.0001$).
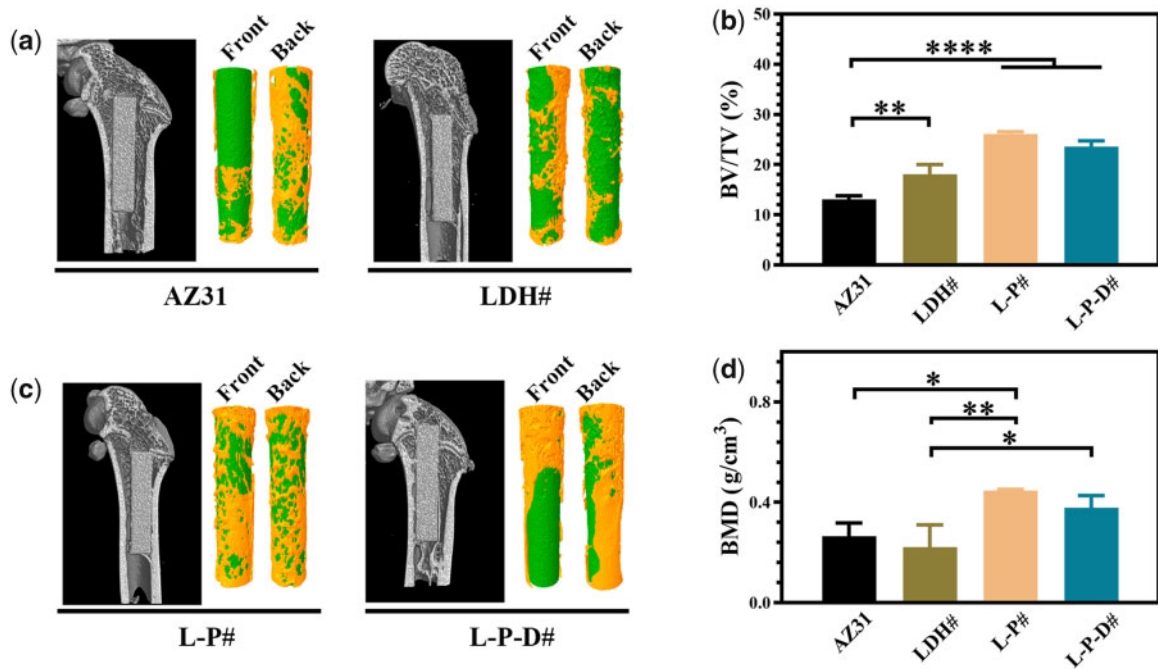

Figure 8. Micro-CT images and the corresponding three-dimensional reconstruction results of AZ31, LDH#, L-P#, and L-P-D# samples after implanted for 8 weeks (a); calculated BV/TV and BMD values of AZ31, LDH#, L-P#, and L-P-D# groups after implanted for 8 weeks (b) (*$P < 0.05$, **$P < 0.01$, ***$P < 0.001$, ****$P < 0.0001$).
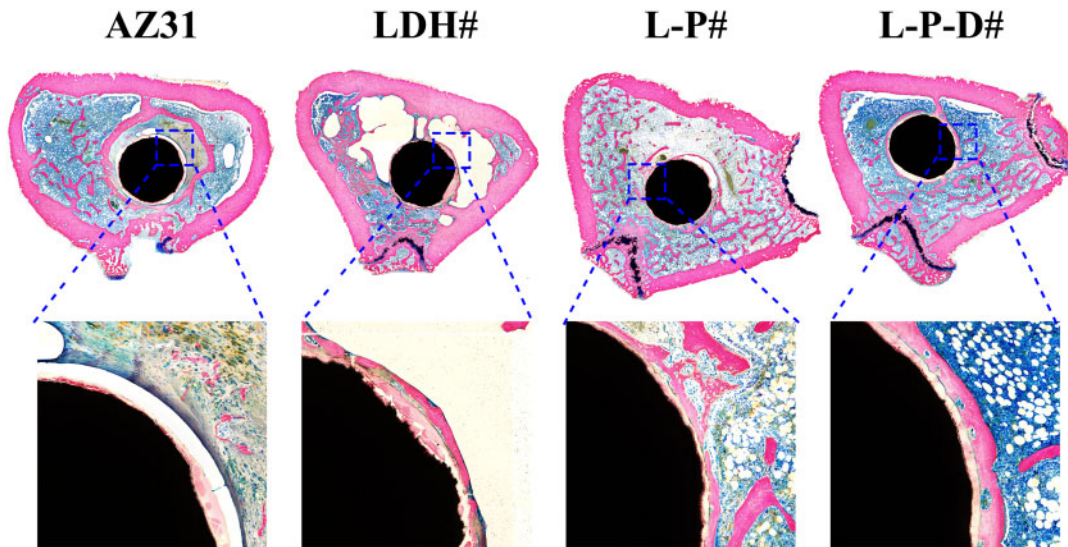
Figure 9. VG staining of AZ31, LDH#, L-P#, and L-P-D# groups after implanted into bone femur for 8 weeks.

The extracts of various samples were collected and then used to culture C3H10T1/2 cells. According to the CCK-8 results, the cells exhibited poor proliferation in the AZ31 group, whereas no toxic effects were observed in LDH# and L-P# groups (Supplementary Fig. S5). As for L-P-D# group, the cell proliferation was inhibited after 7 days of cultivation, suggesting a slight cytotoxicity of Dox to C3H10T1/2 cells. The quantitative and quantitative results of ALP activity are presented in Fig. 7a and b, respectively. At Day 3, the expression levels of ALP activity for all the groups were the same. After culturing for 7 days, L-P# group showed a higher ALP activity than the other two groups. Figure 7c and d displays the results of ECM mineralization, which is the marker of maturation bone differentiation. Few mineralized nodules were observed in all the groups at Day 7. After further culturing to 14 days, large stained areas of mineralized nodules were observed, and the quantitative results followed the trend: L-P# > L-P-D# > LDH#. Furthermore, the osteogenic genes, including COL-I, OCN, OPN, and RUNX2, were detected by qRT-PCR (Fig. 7e). At Day 3, COL-I, OCN, and OPN genes were up-regulated in L-P# and L-P-D# groups. After continuous culturing to 7 days, all the detected genes were expressed at higher levels in PDA-coated groups than in LDH# group, especially in case of L-P# group. Taking all these results into account, we concluded that the deposition of PDA layer on LDH# (L-P#) enhanced sample's osteogenic induction ability. But further immobilization of Dox on the material (L-P-D#) would decrease the osteogenic induction ability, but still higher than LDH# sample.

Figure 8a shows the Micro-CT images of the samples after implanted into rats for 8 weeks and the corresponding 3D reconstruction results. Only half of the surfaces were covered with new bone for AZ31 and LDH# implants. However, for L-P# and L-P-D# implants, more than 70% surface areas were covered by new bone. Moreover, L-P# implant exhibited highest BV/TV and BMD values among the four groups, followed by L-P-D# implant (Fig. 8b). This indicated that L-P# possessed the best osteogenesis capability. The osteointegration of the samples was investigated through VG staining. As shown in Fig. 9, no new bone was formed but a layer of cavity was observed near AZ31 implant, which might be caused by the fast release of hydrogen from AZ31 substrate. New bone was formed surrounding LDH# implant, but a layer of corrosion product was observed between the implant and new bone, which can be a disadvantage for the implant–bone integration. A continuous layer of new bone was also observed for L-P# implant and less corrosion product was detected between the new bone and the implant than LDH# did. Because the corrosion resistance of L-P# sample was better than LDH# sample, less corrosion product was produced. For L-P-D# sample, new bone was formed, but it was not closely bonded on the implant surface. The released Dox from L-P-D# sample was slightly toxic to cells (Supplementary Fig. S5), and hence the bone cells could not grow well on the sample surface, resulting in a gap between the implant and new bone. Nevertheless, compared with AZ31 and LDH# implants, more new bone was observed surrounding L-P-D# implant, indicating a better osteointegration performance.

Conclusions

In this study, a mussel-inspired bifunctional multi-layer film was successfully prepared on Mg alloy. The PDA coated Mg alloy showed enhanced corrosion resistance and photothermal effect under NIR irradiation. The release of Dox from the coated Mg alloy could be controlled by pH adjustment and NIR irradiation. The combination of chemotherapy and thermal therapy significantly decreased the cell viability of osteosarcoma cells *in vitro* and inhibited tumor growth in nude mice. Furthermore, the PDA coated samples improved the ALP activity, ECM mineralization, and osteogenic genes expression in C3H10T1/2 cells *in vitro* and stimulated bone regeneration in rats. Therefore, with the controllable tumor ablation capability to decrease the risk of tumor recurrence and enhanced bone rebuilding performance to repair bone defects, the novel designed bifunctional Mg alloy has potential to be utilized in tumor-related orthopedic implants.

Supplementary data

Supplementary data are available at *REGBIO* online.

Acknowledgements

References

1. Dukan R, Mascard E, Langlais T *et al*. Long-term outcomes of non-invasive expandable endoprostheses for primary malignant tumors around the knee in skeletally-immature patients. *Arch Orthop Trauma Surg* 2021;DOI: 10.1007/s00402-020-03712-z.

2. Cho HS, Han H, Yoon J. Treatment of malignant bone tumor: limb salvage surgery using metallic tumor prosthesis. *J Korean Med Assoc* 2020;**63**:471–6.

3. Outani H, Takenaka S, Hamada K *et al*. A long-term follow-up study of extracorporeal irradiated autografts in limb salvage surgery for malignant bone and soft tissue tumors: a minimum follow-up of 10 years after surgery. *J Surg Oncol* 2020;**121**:1276–82.

4. Han G, Bi WZ, Xu M *et al*. Amputation versus limb-salvage surgery in patients with osteosarcoma: a meta-analysis. *World J Surg* 2016;**40**:2016–27.

5. Das G, Bannoth S, Borthakur BB *et al*. An initial experience of shoulder resections and reconstruction for bone tumours from a cancer centre in North-East India. *Indian J Surg Oncol* 2021;**12**:358–64.

6. Takano M, Sugahara K, Koyachi M *et al*. Maxillary reconstruction using tunneling flap technique with 3D custom-made titanium mesh plate and particulate cancellous bone and marrow graft: a case report. *Maxillofac Plast Reconstr Surg* 2019;**41**:43.

7. Accadbled F, Lemoine CT, Poinsot E *et al*. Bone reconstruction after malignant tumour resection using a motorized lengthening intramedullary nail in adolescents: preliminary results. *J Child Orthop* 2019;**13**:324–9.

8. Gu X-N, Li S-S, Li X-M *et al*. Magnesium based degradable biomaterials: a review. *Front Mater Sci* 2014;**8**:200–18.

9. Zheng YF, Gu XN, Witte F. Biodegradable metals. *Mat Sci Eng R* 2014;**77**:1–34.

10. Kamrani S, Fleck C. Biodegradable magnesium alloys as temporary orthopaedic implants: a review. *Biometals* 2019;**32**:185–93.

11. Zhao D, Witte F, Lu F *et al*. Current status on clinical applications of magnesium-based orthopaedic implants: a review from clinical translational perspective. *Biomaterials* 2017;**112**:287–302.

12. Wang JL, Xu JK, Hopkins C *et al*. Biodegradable magnesium-based implants in orthopedics – a general review and perspectives. *Adv Sci* 2020;**7**:1902443.

13. Zan R, Ji WP, Qiao S *et al*. Biodegradable magnesium implants: a potential scaffold for bone tumor patients. *Sci China Mater* 2021;**64**:1007–20.

14. Chen Y, Xiao M, Zhao H *et al*. On the antitumor properties of biomedical magnesium metal. *J Mater Chem B* 2015;**3**:849–58.

15. Ma N, Chen YM, Yang BC. Magnesium metal – a potential biomaterial with antibone cancer properties. *J Biomed Mater Res A* 2014;**102**:2644–51.

16. Li M, Wang W, Zhu Y *et al*. Molecular and cellular mechanisms for zoledronic acid-loaded magnesium-strontium alloys to inhibit giant cell tumors of bone. *Acta Biomater* 2018;**77**:365–79.

17. Li M, Yao MY, Wang WD *et al*. Nitrogen-containing bisphosphonate-loaded micro-arc oxidation coating for biodegradable magnesium alloy pellets inhibits osteosarcoma through targeting of the mevalonate pathway. *Acta Biomater* 2021;**121**:682–94.

18. Sever MJ, Weisser JT, Monahan J *et al*. Metal-mediated cross-linking in the generation of a marine-mussel adhesive. *Angew Chem Int Ed Engl* 2004;**43**:448–50.

19. Lee H, Dellatore SM, Miller WM *et al*. Mussel-inspired surface chemistry for multifunctional coatings. *Science* 2007;**318**:426–30.

20. Liu X, Zhen Z, Liu J *et al*. Multifunctional MgF2/polydopamine coating on Mg alloy for vascular stent application. *J Mater Sci Technol* 2015;**31**:733–43.

21. Carangelo A, Acquesta A, Monetta T. In-vitro corrosion of AZ31 magnesium alloys by using a polydopamine coating. *Bioact Mater* 2019;**4**:71–8.

22. Wang H, Lin CC, Zhang XR *et al*. Mussel-inspired polydopamine coating: a general strategy to enhance osteogenic differentiation and osseointegration for diverse implants. *ACS Appl Mater Interfaces* 2019;**11**:7615–25.

23. Li H, Jia Y, Peng H *et al*. Recent developments in dopamine-based materials for cancer diagnosis and therapy. *Adv Colloid Interface Sci* 2018;**252**:1–20.

24. Liu Y, Ai K, Liu J *et al*. Dopamine-melanin colloidal nanospheres: an efficient near-infrared photothermal therapeutic agent for in vivo cancer therapy. *Adv Mater* 2013;**25**:1353–9.

25. Ma H, Luo J, Sun Z *et al*. 3D printing of biomaterials with mussel-inspired nanostructures for tumor therapy and tissue regeneration. *Biomaterials* 2016;**111**:138–48.

26. Cheng W, Liang C, Xu L *et al*. TPGS-functionalized polydopamine-modified mesoporous silica as drug nanocarriers for enhanced lung cancer chemotherapy against multidrug resistance. *Small* 2017;**13**:1700623.

27. Peng F, Li H, Wang D *et al*. Enhanced corrosion resistance and biocompatibility of magnesium alloy by Mg-Al-layered double hydroxide. *ACS Appl Mater Interfaces* 2016;**8**:35033–44.

28. Yao QS, Li ZC, Qiu ZM *et al*. Corrosion resistance of Mg(OH)(2)/Mg-Al-layered double hydroxide coatings on magnesium alloy AZ31: influence of hydrolysis degree of silane. *Rare Met* 2019;**38**:629–41.

29. Aga B, Ql A, Lx A *et al*. Tuning the surface immunomodulatory functions of polyetheretherketone for enhanced osseointegration. *Biomaterials* 2020;**230**:119642.

30. Cheng S, Zhang DD, Li M *et al*. Osteogenesis, angiogenesis and immune response of Mg-Al layered double hydroxide coating on pure Mg. *Bioact Mater* 2021;**6**:91–105.

31. Acquesta A, Carangelo A, Monetta T. Degradation of AZ31 magnesium alloy coated with polydopamine film for bio-resorbable implants. *Metall Ital* 2019;**2**:15–20.

32. Chen YQ, Zhao S, Chen MY *et al*. Sandwiched polydopamine (PDA) layer for titanium dioxide (TiO2) coating on magnesium to enhance corrosion protection. *Corros Sci* 2015;**96**:67–73.

33. Sasikala ARK, GhavamiNejad A, Unnithan AR *et al*. A smart magnetic nanoplatform for synergistic anticancer therapy: manoeuvring mussel-inspired functional magnetic nanoparticles for pH responsive anticancer drug delivery and hyperthermia. *Nanoscale* 2015;**7**:18119–28.

34. Yu B, Liu JX, Liu SJ *et al*. Pdop layer exhibiting zwitterionicity: a simple electrochemical interface for governing ion permeability. *Chem Commun* 2010;**46**:5900–2.

35. Cheng F-F, Zhang J-J, Xu F *et al*. pH-sensitive polydopamine nanocapsules for cell imaging and drug delivery based on folate receptor targeting. *J Biomed Nanotechnol* 2013;**9**:1155–63.

36. Lin X, Song X, Zhang Y *et al*. Multifunctional theranostic nanosystems enabling photothermal-chemo combination therapy of triple-stimuli-responsive drug release with magnetic resonance imaging. *Biomater Sci* 2020;**8**:1875–84.

37. Feng C, Lü S, Gao C *et al*. "Smart" fertilizer with temperature- and pH-responsive behavior via surface-initiated polymerization for controlled release of nutrients. *ACS Sustain Chem Eng* 2015;**3**:3157–66.

38. Sun XM, Kaufman PD. Ki-67: more than a proliferation marker. *Chromosoma* 2018;**127**:175–86.

39. Yang C, Zhang J, Ding M *et al*. Ki67 targeted strategies for cancer therapy. *Clin Transl Oncol* 2018;**20**:570–5.

40. Wang Z, Wang XY, Tian Y *et al*. Degradation and osteogenic induction of a SrHPO4-coated Mg-Nd-Zn-Zr alloy intramedullary nail in a rat femoral shaft fracture model. *Biomaterials* 2020;**247**:119962.

41. Sezer N, Evis Z, Koc M. Additive manufacturing of biodegradable magnesium implants and scaffolds: review of the recent advances and research trends. *J Magnes Alloy* 2021;**9**:392–415.